Understanding the Deformation and Fracture of Nitinol using In Situ Synchrotron X-Ray Micro-Diffraction

A. Metha, X.-Y. Gong, V. Imbeni, A. R. Pelton, and R. O. Ritchie

Advanced Materials, vol. 19, May 2007, pp. 1183-1186

2007

DOI: 10.1002/adma.200601916

Understanding the Deformation and Fracture of Nitinol Endovascular Stents Using In Situ Synchrotron X-Ray Microdiffraction**

By *Apurva Mehta*, *Xiao-Yan Gong*, *Valentina Imbeni*, *Alan R. Pelton*, and *Robert O. Ritchie**

Endovascular stents manufactured from superelastic Nitinol represent a major component in the fight against heart disease.[1] However, accurate characterization of the stress/strain distributions in such stents, which govern their deformation and fracture behavior, is essential for their prolonged safe use in human arteries. Nitinol, a nearly equiatomic alloy of nickel and titanium, can "remember" a previous shape and can recover strains as high as 10 % by deformation (superelasticity) or temperature change (shape memory).[2a] These properties result from a reversible first-order phase transition between austenite (cubic, B2) and martensite (monoclinic, B19′).[3] As such, deformation mechanisms of Nitinol are more complex than the conventional modes of plastic deformation in traditional alloys.[4] Consequently, the mechanical behavior of Nitinol under multiaxial conditions remains poorly understood.[5]

[*] Prof. R. O. Ritchie
Department of Materials Science & Engineering
University of California
Berkeley, CA 94720 (USA)
E-mail: roritchie@lbl.gov
Dr. A. Mehta
SSRL/SLAC
Stanford University
Menlo Park, CA 94025 (USA)
Dr. X.-Y. Gong
Medical Implant Mechanics, LLC
Fremont, CA 94539 (USA)
Dr. V. Imbeni
SRI International
Menlo Park, CA 94025 (USA)
Dr. A. R. Pelton
Nitinol Devices & Components
Fremont, CA 94539 (USA)

[**] This work was supported by Nitinol Devices & Components, Inc. (NDC), a Johnson & Johnson Co., by the National Science Foundation under Grant No. CMS-980006 (for R.O.R.), and by the U.S. Department of Energy under Contract No. DE-AC02-76SF00515 (for A.M.). The microdiffraction results were obtained at beamline 7.3.3 at the Advanced Light Source at the Lawrence Berkeley National Laboratory, which is supported by the Director, Office of Science, Office of Basic Energy Sciences, of the U.S. Department of Energy under Contract No. DE-AC02-05CH11231. We are very grateful to Dr. Nobumichi Tamura (of ALS/LBNL) for his help and guidance in collecting and processing the finite-element analysis data and to Dr. Brad L. Boyce (Sandia National Laboratory) for designing and fabricating the in situ straining rig. We are also very grateful to Dr. Scott W. Robertson (University of California, Berkeley) and Dr. Monica Barney (NDC) for helping us run the beamline.

Nevertheless, because of these unique mechanical characteristics, in combination with excellent biocompatibility, Nitinol is used as self-expanding endovascular stents to scaffold diseased peripheral arteries.[4] First-generation Nitinol stents were designed to provide sufficient scaffolding forces to hold open vessels, yet provide enough elasticity to "breathe" with pulsatile pressure differentials from the cardiac cycle. A variety of clinical studies indicate that these stents perform this primary function quite well.[1,6,7] More recent in-depth studies, however, reveal that superficial femoral arteries (SFAs) are subjected to complex in vivo multiaxial deformation with up to 60 % rotation and ca. 20 % contraction in the SFA as the leg is bent from an extended position.[8] Correspondingly, during a walking cycle, a stent deployed in the SFA undergoes severe multiaxial displacements from pulsatile motion (ca. 4×10^7 cycles annually) plus bending, torsion, and axial motions (at a rate of ca. 1×10^6 cycles annually).[9] Although there are ca. 40 times more cardiac displacement cycles, the combined nonpulsatile motions result in far greater cyclic strain magnitudes, and therefore, have the possibility of inducing greater fatigue damage.

Stent design for these "dynamic" arteries and subsequent prediction of conditions and locations of likely fatigue-induced fracture events is invariably performed with detailed finite-element analysis.[10] These numerical models attempt to incorporate the nonlinear mechanical properties of the Nitinol constitutive relationship to provide an estimate of the distributions of local stresses and strains. Nevertheless, endovascular stents still fracture in vivo![11] Accordingly, we may conclude that either our knowledge of the nature and magnitude of the deformation of a stented artery is incomplete, or current finite-element models fail to fully represent the actual mechanical response of a Nitinol stent.

Deformation of a Nitinol stent (e.g., Fig. 1a) due to in vivo loading conditions can be modeled with bending and unbending of the repeating structural "half diamonds". To simulate these stent features, our test sample consists of a planar object composed of two opposed half diamonds that we refer to as a "diamond specimen" (Fig. 1b).[12] These diamonds contain the salient geometric features of many Nitinol self-expanding stents, and are thus the ideal configuration for fundamental strain and fatigue[12] analyses.

The computed ε_{yy} components of the deviatoric strain tensor in the diamond from the synchrotron Laue microdiffraction experiments are shown in Figure 2. Under 0 mm displace-

ADVANCED MATERIALS

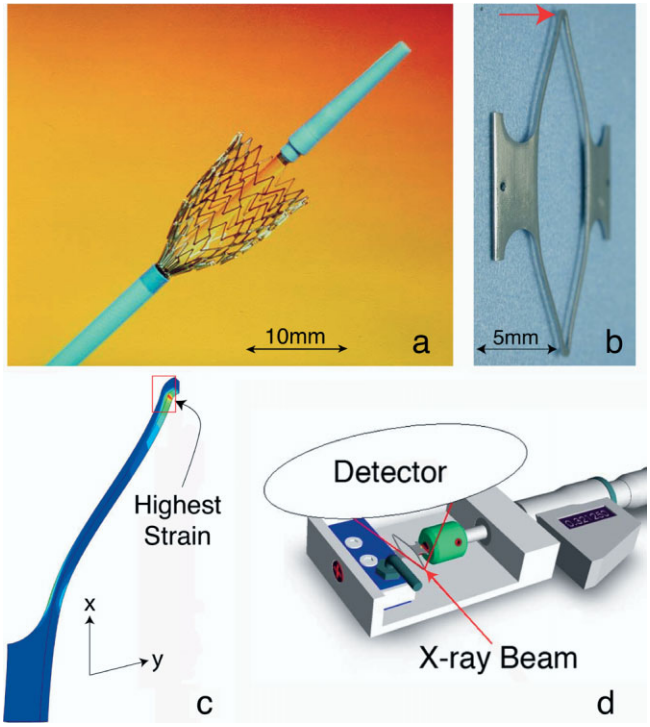

Figure 1. a) An image of a Cordis S.M.A.R.T. Nitinol self-expanding stent that illustrates the repeating pattern of "half diamonds" that make up each row of the 3D structure. b) The Nitinol diamond stent-like specimen used for the diffraction studies closely resembles the "half-diamond" structure of the stent shown in (a). This diamond specimen is based on the S.M.A.R.T. stent geometry and therefore has scaled stent dimensions of strut length (8 mm), strut width (330 μm), and strut thickness (350 μm) as described elsewhere [11]. The red arrow illustrates the location of the 400 μm × 500 μm region of the sample that is scanned in the diffraction experiments. When the upper and lower tabs are pulled apart, the sample is considered to be under tensile deformation. This scanned region is also superimposed on the quarter symmetry finite-element model of the diamond in (c). d) A schematic drawing of the custom straining rig used in the in situ X-ray diffraction straining experiments. The X-ray beam is scanned across the edge of the diamond strut with the resultant individual diffraction patterns collected by a charge-coupled device (CCD) detector.

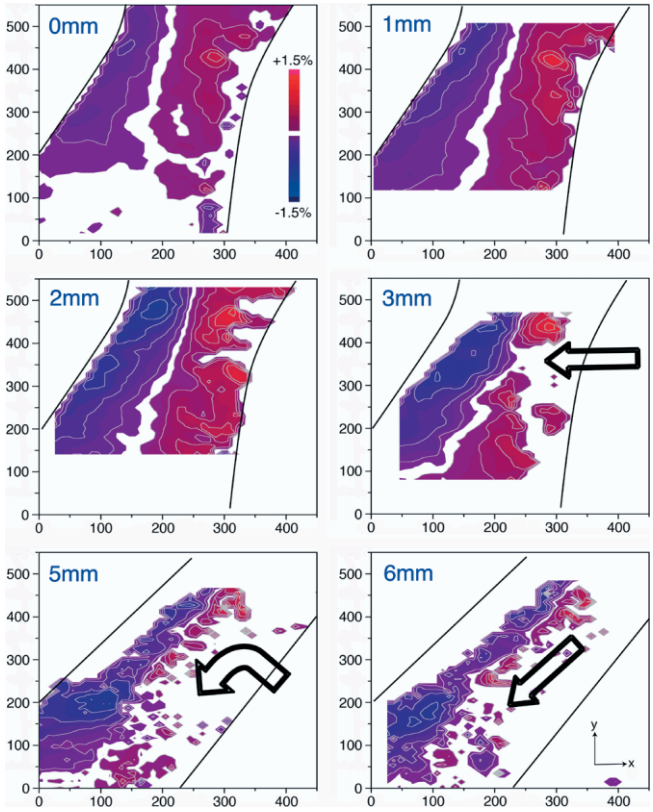

Figure 2. Maps of the deviatoric strain of the B2 austenite along the vertical *y* axis (ε_{yy}) from X-ray diffraction analysis of the corresponding 400 μm × 500 μm scanned region marked with the red arrow in Figure 1b. The numeric scales are in units of micrometers. The global displacement for these maps is shown in the upper left corner of each image. The dark lines illustrate the approximate location of the edges of the diamond strut. The red color indicates tensile strain whereas blue indicates compressive strain; note also the presence of a white neutral axis. The maximum local strain in austenite was measured to be ±1.5 %. Above this strain, austenite transforms to martensite, which is not analyzed here, but can be inferred from where the austenite disappears. Martensite generally initiates at the surfaces with the highest applied deformation and begins to move toward the center of the diamond strut, as indicated by the arrows in the 3 mm, 5 mm, and 6 mm maps. However, it is observed that, even at 6 mm deformation, there is a region of strain-stabilized austenite retained along the center of the strut that resists transformation. Consequently, the martensite transformation front moves down along the strut edge as deformation strains increase.

ment, the specimen is austenitic, but there are regions with residual strain, presumably from processing. Note the existence of a well-defined neutral axis (white) that separates the compressive (blue) regions from the tensile (red) regions. At 2 mm displacement (ca. 2 % local strain), the highest locally strained regions of the diamond specimens begin to transform to martensite.[2b] For this analysis, the martensitic regions can be readily identified by comparison of the maps and noting where the austenite has "disappeared". Consistent with theory,[3] the maximum local strain in the austenite is 1.5 %, even with up to the highest deformations studied here. With increasing deformation, there is an increase in the volume fraction of stress-induced martensite. The figures also reveal subgrains with compressive strain surrounded by larger tensile regions as the applied deformation is increased. Similar results are obtained for the computed ε_{xx} components of the deviatoric strain tensor, not shown in this Communication.

Figure 3 shows the resultant ε_{yy} strain field component predicted by the finite-element analysis. The continuum-based model predicts smooth transitions between regions of tensile and compressive strains, with a maximum local strain of 1.5 %. Furthermore, the finite-element analysis indicates that the martensitic transformation initiates at surfaces with an increase in transformed volume fraction with increasing deformation.

Comparison between Figures 2 and 3 highlights the differences in fine detail between the two independent strain analyses; these differences dramatically increase at the higher deformation values. For example, in contrast to the finite-element predictions, nonuniform strain gradients were observed

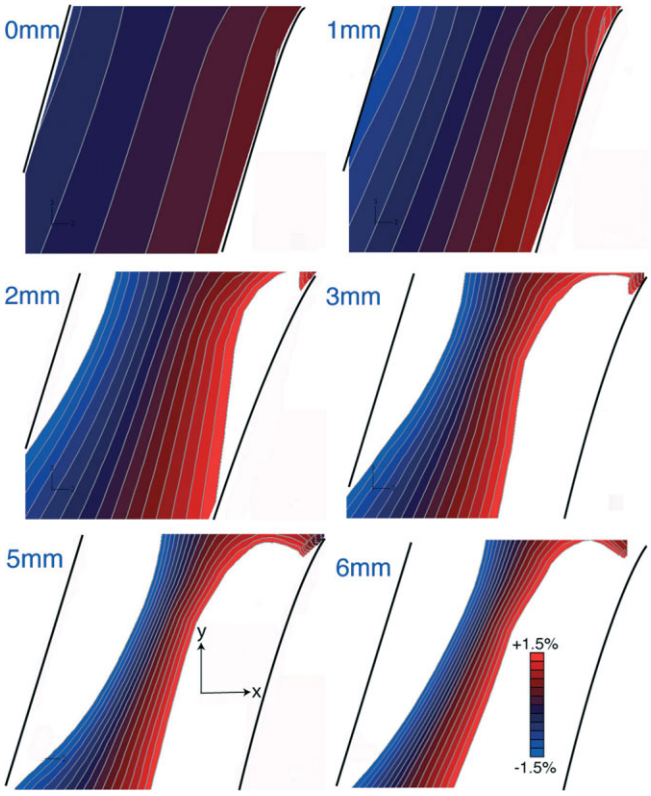

Figure 3. Maps of the deviatoric strain of the B2 austenite along the vertical *y* axis (ε_{yy}) from finite-element modeling corresponding to the 400 μm × 500 μm scanned region in Figure 1c. The global displacement for these maps is shown in the upper left corner of each image. The dark lines illustrate the approximate location of the edges of the diamond strut. The red color indicates tensile strain whereas blue indicates compressive strain; the maximum local strain in austenite is ±1.5 %, consistent with the diffraction measurements. Unlike the strain analysis in Figure 2, however, the computational model shows continuous strain gradients across the diamond strut. Furthermore, this model shows that martensite gradually consumes the austenite phase in the center of the strut as the deformation strains increase.

experimentally. Furthermore, the diffraction-based analysis indicates that the surface-nucleated martensite regions advance towards each other with increasing deformation. However, contrary to the model predictions, there remains a spine of retained austenite in the middle of the strut even at the highest deformation studied here. Accordingly, it is observed that the transformation front moves down the length of the strut rather than moving towards the middle (3–5 mm). Finally, some austenitic subgrains resisted transformation even after the transformation front progressed through the region.

The most likely explanation for these differences can be associated with the strain-accommodation process from the martensitic transformation. Phase transitions are accompanied with a concomitant decrease of free energy; therefore, it is logical that martensite nucleates at regions of highest local strain. However, the local strain fields are nonuniform due to influences from lattice-induced strain, grain boundaries, dislocations, inclusions, grain orientations, or internal strain fields. Therefore, the martensitic transformation relieves strain on a submicrometer scale. Consequently, as each austenite grain transforms to martensite, there is a redistribution of the local strain fields that results in a change in the position and direction of the strain propagation. One possible explanation for the observed distribution of strain is based on the difference (factor of two) in the austenite and martensite moduli.[12,13] This effect alone could certainly modify the load-carrying capacity of the two-phase structures, thereby providing a potent driving force for the strain redistribution. The experimental observation of redirection of the transformation front has very important implications for strut fractures in Nitinol stents. At relatively low displacements, if the local strain field encounters a sufficiently large flaw, the defect will induce the strain field to grow such that the material may fracture at the location predicted by the finite-element model. In the absence of flaws of critical dimension near the initial high stress location, the transformation front, which has now changed direction, will begin to propagate down the length of the strut. As the propagating strain front runs down the length of the strut, fracture may occur at locations significantly different from those suggested by the finite-element model. It is noted that recent Nitinol-based finite-element models integrate crystallographic effects such as texture and grain size.[14–17] However, even these newest models have not been shown to explain fully the multiaxial modes of deformation. Consequently, it is imperative that finite-element models incorporate the more accurate and independent strain distributions afforded by high-resolution microdiffraction.

In summary, the first direct in situ X-ray microdiffraction measurements inside the synchrotron of the local strain field (at 10 μm resolution) of a stent-like Nitinol component subjected to realistic multiaxial loading are reported. Our micro-diffraction measurements indicate that state-of-the-art commercial finite-element models are sufficient for predicting local strain fields up to 3 %. However, there are significant discrepancies between measured and calculated strains at larger displacements that result from the continuum-mechanics-based model predictions. Consequently, it is imperative that future development of finite-element models must incorporate effects of transformational strain, phase redistribution, and plastic strain to provide higher fidelity predictions of Nitinol stent performance in vivo.

Experimental

Diamond specimens (Fig. 1b) were laser machined from a Ti-50.8 at % Ni microtube (4.7 mm outer diameter, 0.4 mm wall thickness). Typical grain sizes were ca. 10 nm, and were thus difficult to analyze with white-beam Laue diffraction techniques; therefore, diamond specimens were annealed at 850 °C (30 min) to give an austenitic microstructure with ca. 20–50 μm grain size. It is well known that thermomechanical processing of Nitinol strongly affects grain size and thus the resultant mechanical properties; nevertheless, these initial investigations on annealed specimens serve to establish the experimental methodology and important predictions of strain analysis.

ADVANCED MATERIALS

We deformed the diamond samples in the "tensile mode", where the tabs were pulled apart such that the top edge of the strut arm was in compression and the inner edge was under tension (refer to Fig. 1c). The custom-designed straining rig (Fig. 1d) was placed on a high-precision *x*–*y*–*z* stage on the microdiffractometer at the Advanced Light Source (beamline 7.3.3, Lawrence Berkeley National Laboratory) at an angle of 45° to the incident beam in the vertical plane. A MAR1600 X-ray charge-coupled device (CCD) was placed at 90° to the incident beam, with beamline optics adjusted so that a 1 μm × 1 μm spot with an X-ray spectrum of 5–14 keV was incident on the sample [18]. A 500 μm × 400 μm region, enclosing the location of the highest strains on the edge of the diamond strut, was scanned in situ by moving the rig with respect to the X-ray beam for each deformation condition. A white-beam Laue pattern from austenite [19] was collected at each point of the grid and was subsequently analyzed using the program XMAS [20]. The deviation of the diffraction pattern from the cubic symmetry was transformed into a 3 × 3 deviatoric strain tensor. These experiments were repeated several times and the results presented herein are considered representative of the deformation behavior of Nitinol.

Finite-element computations were performed with a commercial finite-element software package, ABAQUS/Standard version 6.4-1, in combination with a specialized user-defined material subroutine (UMAT), to model the nonlinear mechanical properties of Nitinol. The Nitinol UMAT incorporates the uniaxial tension–compression asymmetry, austenite and martensite moduli, as well as effects of plasticity [13, 21, 22]; however, other, more complex unique material behavior, such as nonproportional triaxial stress states, are not specifically included in the model. Rather, generalization to a multiaxial stress state is based on generalized plasticity theory. For direct comparison with the experiment, a user-defined variable subroutine was developed to compute the deviatoric strain fields.

Received: August 23, 2006
Revised: October 19, 2006
Published online: April 13, 2007

[1] M. Schillinger, S. Sabeti, C. Loewe, P. Dick, J. Amighi, W. Mlekusch, O. Schlager, M. Cejna, J. Lammer, E. Minar, *N. Engl. J. Med.* **2006**, *354*, 1879.

[2] a) Conventional metallic alloys typically elastically deform to no more than 1 %. b) The transformed martensite needles are significantly smaller than the incident X-ray beam. Consequently, single-crystal diffraction patterns were not obtained from the martensite

[3] C. M. Wayman, T. W. Duerig, in *Engineering Aspects of Shape Memory Alloys* (Eds: T. W. Duerig, K. N. Melton, D. Stöckel, C. M. Wayman), Butterworth-Heinemann, Oxford **1990**, p. 3.

[4] T. W. Duerig, A. R. Pelton, D. Stöckel, *Mater. Sci. Eng. A* **1999**, *273–275*, 149.

[5] J. M. McNaney, V. Imbeni, Y. Jung, P. Papadopoulos, R. O. Ritchie, *Mech. Mater.* **2003**, *35*, 969.

[6] S. H. Duda, B. Pusich, G. Richter, P. Landwehr, V. L. Oliva, A. Tielbeek, B. Wiesinger, J. B. Hak, H. Tielemans, G. Ziemer, E. Cristea, A. Lansky, J. P. Bérégi, *Circulation* **2002**, *106*, 1505.

[7] S. H. Duda, M. Bosiers, J. Lammer, D. Scheinert, T. Zeller, A. Tielbeek, J. Anderson, B. Wiesinger, G. Tepe, A. Lansky, C. Mudde, H. Tielemans, J. P. Bérégi, *J. Vasc. Interv. Radiol.* **2005**, *16*, 331.

[8] C. P. Cheng, N. M. Wilson, R. L. Hallett, R. J. Herfkens, C. A. Taylor, *J. Vasc. Interv. Radiol.* **2006**, *17*, 979.

[9] M. Silva, *J. Anthroplasty* **2002**, *17*, 693.

[10] X.-Y. Gong, A. R. Pelton, T. W. Duerig, N. Rebelo, K. Perry, in *Proc. of SMST-2003* (Eds: A. R. Pelton, T. W. Duerig), SMST Society, Pacific Grove, CA **2004**, 453.

[11] D. Allie, C. Herbert, C. Walker, *Endovasc. Today* **2004**, July/August, 22.

[12] A. R. Pelton, X.-Y. Gong, T. W. Duerig, in *Proc. of SMST-2003* (Eds: A. R. Pelton, T. W. Duerig), SMST Society, Pacific Grove, CA **2004**, 293.

[13] N. Rebelo, X.-Y. Gong, M. Connally, in *Proc. of SMST-2003* (Eds: A. R. Pelton, T. W. Duerig), SMST Society, Pacific Grove, CA **2004**, 501.

[14] Y. Jung, P. Papadopoulos, R. O. Ritchie, *Int. J. Numer. Meth. Eng.* **2004**, *60*, 429.

[15] P. Thamburaja, L. Anand, *J. Mech. Phys. Solids* **2001**, *49*, 709.

[16] P. Thamburaja, L. Anand, *Int. J. Plast.* **2002**, *18*, 1607.

[17] P. Thamburaja, L. Anand, *Acta Mater.* **2003**, *51*, 325.

[18] N. Tamura, R. Spolenak, B. C. Valek, A. Manceau, M. Meier Chang, R. S. Celestre, A. A. MacDowell, H. A. Padmore, J. R. Patel, *Rev. Sci. Instrum.* **2002**, *73*, 1369.

[19] X. Huang, G. J. Ackland, K. M. Rabe, *Nat. Mater.* **2003**, *2*, 307.

[20] a) N. Tamura, A. A. MacDowell, R. Spolenak, B. C. Valek, J. C. Bravman, W. L. Brown, R. S. Celestre, H. A. Padmore, B. W. Batterman, J. R. Patel, *J. Synchrotron Radiat.* **2003**, *10*, 137. b) XMAS manual. http://xraysweb.lbl.gov/microdif/downloads/XMAS%20Manual%20v1.pdf (accessed March 2006).

[21] N. Rebelo, N. Walker, H. Foadian, in *Simulation of Implantable Nitinol Stents, Abaqus Users' Conf.*, ABAQUS Inc., Providence, RI **2001**, 1.

[22] X.-Y. Gong, A. R. Pelton, *Proc. of SMST-2003* (Eds: A. R. Pelton, T. W. Duerig), SMST Society, Pacific Grove, CA **2004**, 443.

